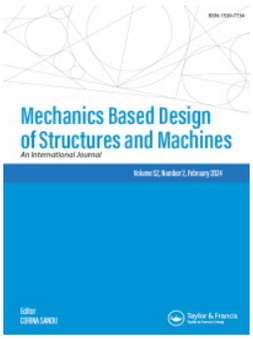

Taylor & Francis
Taylor & Francis Group

Mechanics Based Design of Structures and Machines
An International Journal

ISSN: 1539-7734 (Print) 1539-7742 (Online) Journal homepage: www.tandfonline.com/journals/lmbd20

Analysis of cutting forces at different spindle speeds with straight and helical-flute tools for conventional-speed milling incorporating the effect of tool runout

Mehmet Aydın & Uğur Köklü

To cite this article: Mehmet Aydın & Uğur Köklü (2024) Analysis of cutting forces at different spindle speeds with straight and helical-flute tools for conventional-speed milling incorporating the effect of tool runout, Mechanics Based Design of Structures and Machines, 52:2, 867-893, DOI: 10.1080/15397734.2022.2125878

To link to this article: https://doi.org/10.1080/15397734.2022.2125878

MECHANICS BASED DESIGN OF STRUCTURES AND MACHINES
2024, VOL. 52, NO. 2, 867–893
https://doi.org/10.1080/15397734.2022.2125878

Analysis of cutting forces at different spindle speeds with straight and helical-flute tools for conventional-speed milling incorporating the effect of tool runout

Mehmet Aydın[a] and Uğur Köklü[b]

[a]Department of Industrial Design, Bilecik Şeyh Edebali University, Bilecik, Turkey; [b]Department of Mechanical Engineering, Karamanoğlu Mehmetbey University, Karaman, Turkey

ABSTRACT

This paper is concerned with the experimental investigation and mechanistic prediction of cutting forces for flat-end milling with tool runout. The effects of the tool geometry, the workpiece material and cutting parameters such as spindle speed, tool engagement and cutting direction are investigated. The mechanistic force model uses the trochoidal flute path to calculate the undeformed chip thickness. Average cutting force and linear regression model are applied for identifying the coefficients of the force model, and tool runout parameters are established from the radii of all flutes at the free end of the cutting tool. A series of milling processes are conducted on AZ31 Magnesium (Mg) alloy and titanium alloy (Ti6Al4V) to analyze the instantaneous cutting force curves, amplitudes of cutting forces and peak forces over a wide range of conventional spindle speeds, namely 600, 1200 and 3000 rev/min. It is found that the values of the cutting force coefficients are higher at lower spindle speed and decrease with an increase in spindle speed, especially when machining Ti6Al4V alloy. For the edge force coefficients, it is observed a slight variation when using cutting tools with different helix angles. Besides, the cutting force amplitudes strongly depend upon the workpiece material. The helix angle has a significant influence on the transverse force amplitude at the spindle speed of 600 rev/min. The cutting forces obtained mechanistically are also substantiated by comparison with measurements.

ARTICLE HISTORY
Received 22 June 2022
Accepted 12 September 2022

KEYWORDS
End milling; coefficients; forces; mechanistic model; tool geometry; runout

1. Introduction

End milling is one of the extensively utilized complex manufacturing methods in metalworking industries. Tool runout occurs from several sources such as tool axis offset, tool axis tilt and setting of inserts in end milling operations, which affects the instantaneous undeformed chip thickness and cutting forces depending on the cutting conditions and cutting geometry (Li and Li 2005). A large number of predictive cutting force models have been developed to examine the milling process, which focus on physical aspects. However, some fundamental physical phenomena are still difficult to understand in a wide range of cutting conditions. Thus, it seems interesting to analyze the physical phenomena with the help of cutting force modeling in various conditions.

Modeling of cutting forces in end milling constitutes the basis for predicting process stability (Hong et al. 2003), identifying surface location errors (Aydın et al. 2015) and analyzing surface generation (Islam, Lee, and Cho 2008). There are three different approaches to predict cutting forces in milling processes: analytical, numerical and mechanistic (Ehman et al. 1997), where the

CONTACT Mehmet Aydın mehmet.aydin@bilecik.edu.tr Department of Industrial Design, Bilecik Şeyh Edebali University, Bilecik, Turkey.
Communicated by Francesco Tornabene.

situations of tool runout are considered. The analytical models relate cutting forces to process variables and mechanical aspects. Armarego and Deshpande (1993) proposed a force model using oblique cutting analyses. In this model, they discussed the effects of deflection and tool eccentricity. Li and Li (2004) developed another model including the effects of runout to predict milling forces applying Oxley's machining theory. In their model, the action of an individual flute segment was described as oblique cutting. Wang and Liang (1996) proposed an analytical formulation to compute the chip load in milling processes with the effect of runout. In this formulation, the cutting geometry was modeled based on the circular flute trajectory. While this approximation greatly simplifies the analysis, it causes significant errors. Otherwise, advances in computers have led to the development of numerical methods, where the relationship between tool geometry and workpiece is studied with the finite element-based models (Mackerle 2003).

In mechanistic model, cutting forces are proportional to undeformed chip area (Altintas 2000). Kline and DeVor (1983) presented a mechanistic model to predict milling forces for the cutting geometry with tool runout. They calibrated the empirical coefficients with the measured average forces and an undeformed chip thickness approach, which are referred to as force coefficients. Based on a similar mechanistic cutting force model considering the cutter edge trajectories with runout effect, Lu et al. (2018) determined the cutting forces for micro flat-end milling. A general approach was established by Wan and Zhang (2006) for cutting force prediction in milling operations, who included the influences of the tool and workpiece and immersion angle variation. Montgomery and Altintas (1991) proposed a theoretical cutting force method which describes the undeformed chip thickness from the trochoidal motion of the tool. Recently, Wojciechowski (2015) investigated cutting forces in ball-end milling of inclined surfaces by including the effect of surface inclination and tool runout. However, in die and mold making operations, where cutting conditions change, a variety of cut tests are necessary to determine the cutting forces. Considering the cutting tool, workpiece and cutting parameters, a systematic investigation of the influences of tool runout on the milling process based upon trochoidal flute trajectories should be performed.

There are mainly two approaches for identifying the force coefficients, i.e., mechanistic approach (Aydın et al. 2014; Dikshit, Puri, and Maity 2017; Wang et al. 2021), oblique transformation method (Budak, Altıntaş, and Armarego 1996; Aydın and Köklü 2017, 2020). These approaches require a linear regression of the measured cutting forces over a range of feeds per tooth using a constant cutting speed and depth of cut. Another method employs a nonlinear optimization approach to carry out a least-squares fitting of predicted cutting forces to measured ones, which allows to study the effects of machining parameters on dynamic cutting forces (Rubeo and Schmitz 2016). By decomposing the cutting forces into nominal and perturbation components, Wan et al. (2007, 2010) also suggested an approach which calibrates simultaneously the force coefficients and tool runout by solving nonlinear equations for flat-end milling.

This paper presents an approach to study the effects of tool geometry, workpiece material and cutting parameters such as spindle speed, tool engagement and cutting direction on the cutting forces for flat-end milling with tool runout. Numerous milling processes are also conducted to determine the instantaneous cutting force curves, amplitudes of cutting forces and peak forces for conventional-speed milling using a mechanistic force model. This model takes the runout into account during the cutting force calculation, and the undeformed chip thickness is calculated from the trochoidal flute path. The force coefficients are derived using average cutting force and linear regression model, and the tool runout parameters are determined by measuring the radii of all flutes at the free end of the end mill.

2. Mechanistic cutting force model

An end milling with a straight-flute end mill is depicted in Fig. 1. The motion of cutting edge is a combination of rotation and translation. The orientation and magnitude of cutting forces

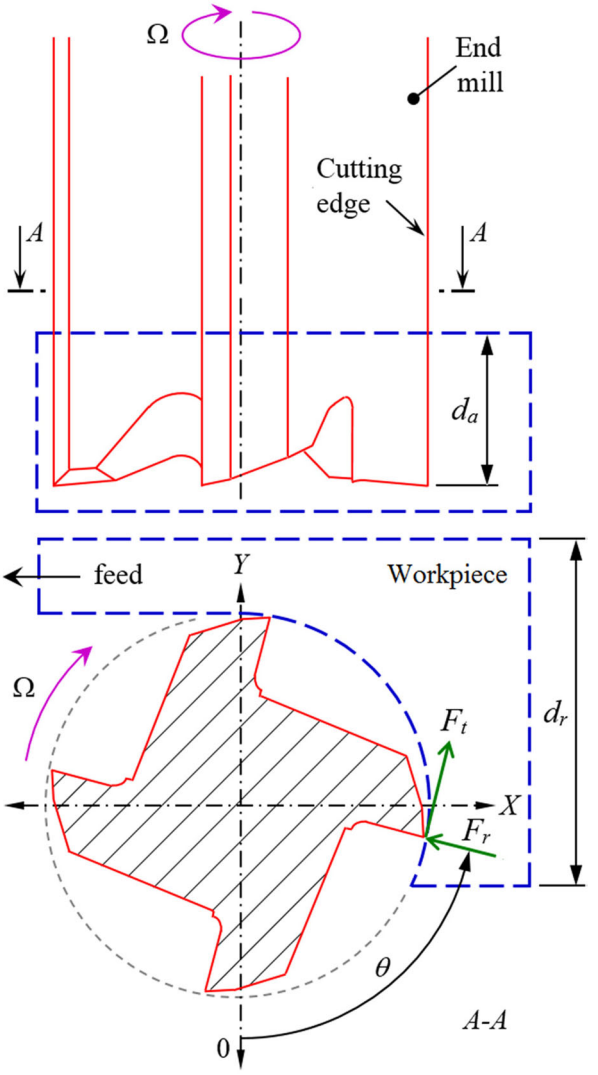

Figure 1. Straight-flute end milling.

change because this relative motion causes a chip geometry that varies with time. Thus, it is required to consider the trajectory of cutting edges to determine forces accurately.

To model the cutting forces for straight-flute end milling, a mechanistic force model is applied, which is proven in the literature (Adem, Fales, and El-Gizawy 2015). In this study, the mechanistic model takes into account the effect of runout on the chip load, and the undeformed chip thickness is calculated from the trochoidal flute trajectories. Tangential (F_t) and radial (F_r) forces applied on the kth flute of a rigid end mill at time t are described by

$$\left.\begin{aligned} F_t^k(t) &= (K_{tc}\, w_k(t) + K_{te})\, d_a \\ F_r^k(t) &= (K_{rc}\, w_k(t) + K_{re})\, d_a \end{aligned}\right\} \tag{1}$$

where K_{tc} and K_{rc} denotes the tangential and radial cutting force coefficients, respectively. K_{te} and K_{re} are the corresponding edge force coefficients. d_a is the axial depth and $w_k(t)$ is the undeformed chip thickness.

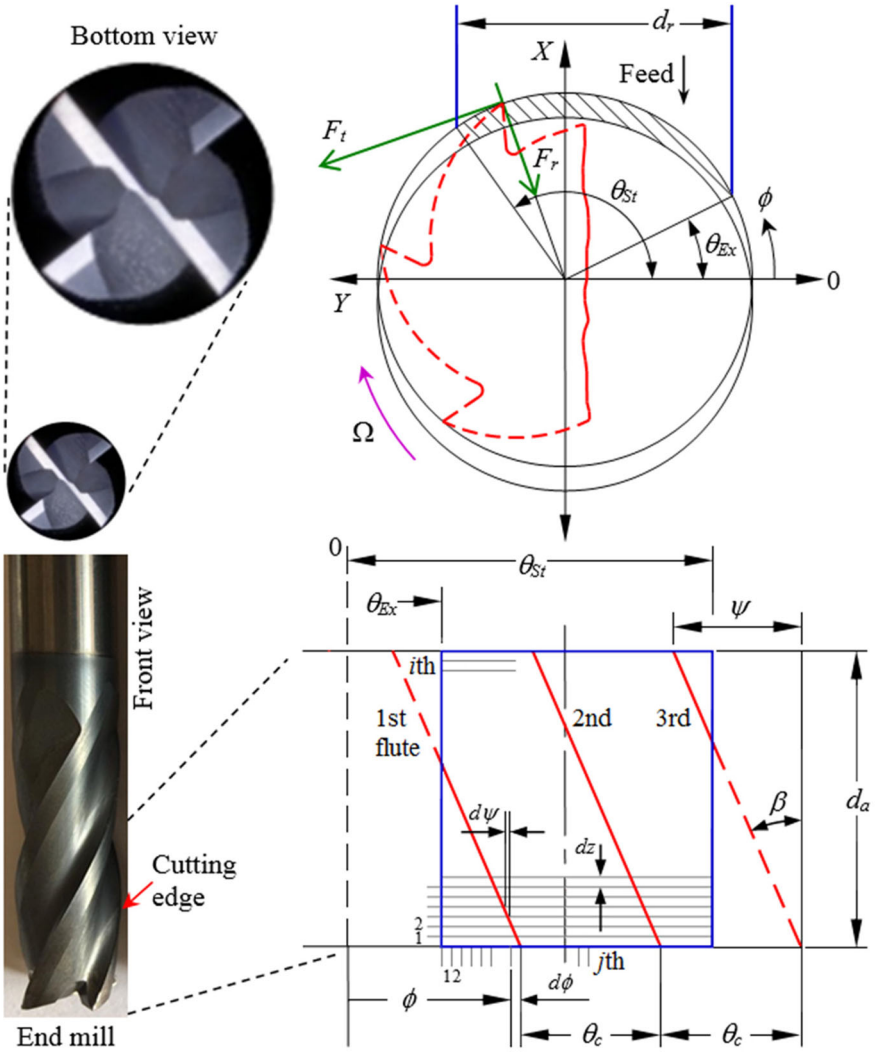

Figure 2. Helical-flute end milling (Tlusty 2000).

The tangential and radial forces are then projected to feed (F_x) and transverse (F_y) force components as

$$\begin{Bmatrix} F_x^k(t) \\ F_y^k(t) \end{Bmatrix} = \begin{bmatrix} \cos\theta_k(t) & \sin\theta_k(t) \\ \sin\theta_k(t) & -\cos\theta_k(t) \end{bmatrix} \begin{Bmatrix} F_t^k(t) \\ F_r^k(t) \end{Bmatrix} \tag{2}$$

where $\theta_k(t)$ is the rotation angle of the kth flute.

The contributions of entire flutes are computed, and are added to achieve the total instantaneous forces on the tool at the current time as follows

$$F_q(t) = \sum_{k=1}^{N_f} F_q^k(t)(q = x, y) \tag{3}$$

where N_f is the flute number.

To consider the effect of helix angle (β), the end mill is discretized into L number of disk elements along its axis, whose elementary length is $dz = d_a/L$, as illustrated in Fig. 2. Considering

the ith disk of the kth flute at the jth angular position of the tool, the immersion angle is expressed as

$$\theta_k(t) = \phi(j) + (k-1)\theta_c + \psi(i) \tag{4}$$

where $\phi(j) = \alpha + j\,d\phi$ is the position angle of flute tip, and is calculated with respect to the initial position angle (α) by indexing the amount of angular increment ($d\phi$). $\theta_c = 2\pi/N_f$ is the pitch angle. The lag angle ($\psi(i)$) is calculated using

$$\psi(i) = i\,dz\,[\tan(\beta)/R] \tag{5}$$

where R is the tool radius.

In helical-flute end milling, the elementary tangential (dF_t) and radial (dF_r) forces are defined as

$$\begin{aligned} dF_t^k(t) &= (K_{tc} w_k(t) + K_{te})\,dz \\ dF_r^k(t) &= (K_{rc} w_k(t) + K_{re})\,dz \end{aligned} \tag{6}$$

Subsequently, the elemental forces are expressed in the Cartesian coordinate system as given below

$$\begin{Bmatrix} dF_x^k(t) \\ dF_y^k(t) \end{Bmatrix} = \begin{bmatrix} \cos\theta_k(t) & \sin\theta_k(t) \\ \sin\theta_k(t) & -\cos\theta_k(t) \end{bmatrix} \begin{Bmatrix} dF_t^k(t) \\ dF_r^k(t) \end{Bmatrix} \tag{7}$$

The total force components applied on the kth flute at time t are evaluated by integrating Eq. (7) along the axial depth

$$F_q^k(t) = \int_0^z dF_q^k(t)dz \;\; (q = x, y) \tag{8}$$

where z is the axial coordinate of the ith disk of the kth flute. Finally, the instantaneous forces are calculated by summing the forces generated by all flutes.

The flowchart for determining the cutting forces in helical-flute end milling simulation is illustrated in Fig. 3. The simulation begins by defining the cutting parameters (spindle speed (Ω), axial depth (d_a), feed rate (f), entry and exit angles (θ_{St}, θ_{Ex}), tool radius (R), number of flutes (N_f), force coefficients) and numerical parameters (initial time and angle values, numbers of time steps (T), angular steps (K) and axial steps (L), time interval (dt), integration angle ($d\phi$)). Then, the program runs the time loop for discretized disks. The program checks for each time interval (dt) whether the angular position of kth flute of the ith disk is in cut or out of cut. If cutting edge is not in cut, the forces are adjusted to zero. Otherwise, the forces in feed and transverse directions (F_x, F_y) are evaluated using Eq. (7). The main loop continuous until the number of simulated time steps equals the predefined one. At the final stage, the program plots the forces.

3. Calibration of force model coefficients

It is necessary to calibrate the force model coefficients to predict cutting forces. There are various methods to calibrate the model coefficients. Here, the force coefficients were derived from the average force components measured during slot cutting experiments which were conducted over a range of feeds per tooth (f_z) with a constant spindle speed and axial depth. Such an experimental method was also used by Zhang, Yu, and Wang (2019). A single-flute end mill was used to eliminate the effects of runout. Projecting the tangential and radial force components into the Cartesian coordinate system and integrating over one revolution yield the following expressions for average cutting forces in feed (X) and transverse (Y) directions (Rubeo and Schmitz 2016).

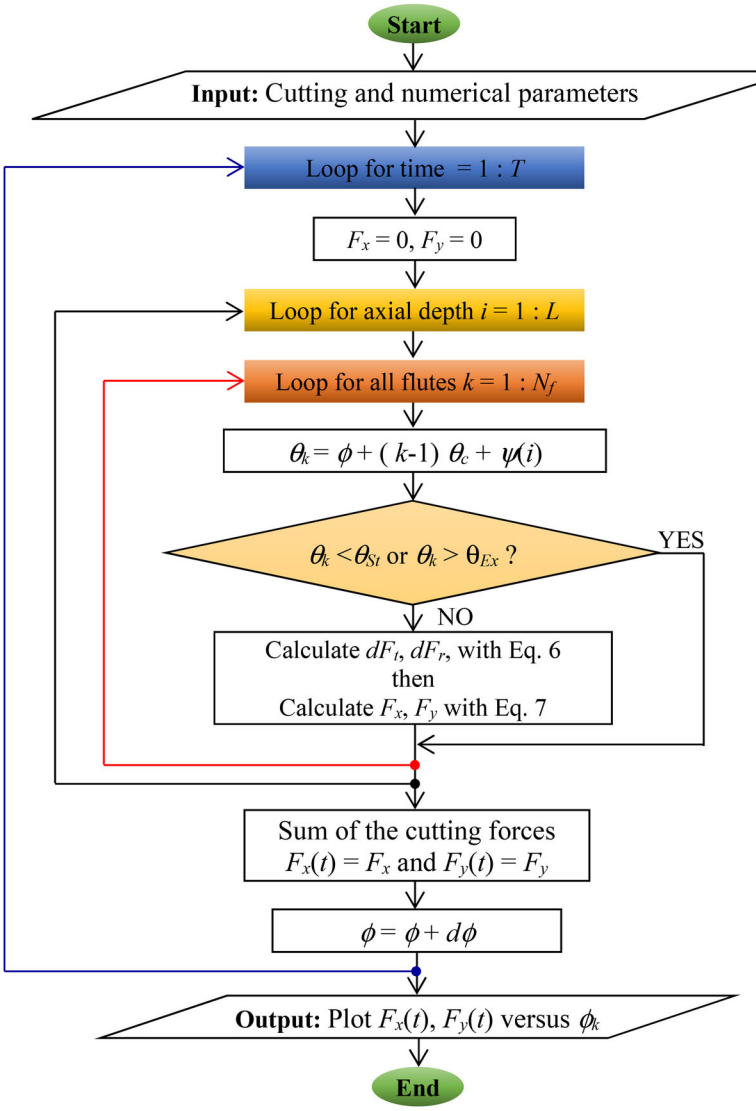

Figure 3. Flowchart for calculating cutting forces in helical-flute end milling.

$$\bar{F}_x = \frac{N_f\, d_a}{8\pi}\{K_{tc}[\cos 2\theta_{St} - \cos 2\theta_{Ex}] + K_{rc}[(2\theta_{Ex} - \sin 2\theta_{Ex}) - (2\theta_{St} - \sin 2\theta_{St})]\} f_z + \frac{N_f\, d_a}{2\pi}\{K_{te}[\sin\theta_{Ex} - \sin\theta_{St}] + K_{re}[\cos\theta_{St} - \cos\theta_{Ex}]\} \tag{9}$$

$$\bar{F}_y = \frac{N_f\, d_a}{8\pi}\{K_{tc}[(2\theta_{Ex} - \sin 2\theta_{Ex}) - (2\theta_{St} - \sin 2\theta_{St})] + K_{rc}[\cos 2\theta_{Ex} - \cos 2\theta_{St}]\} f_z + \frac{N_f\, d_a}{2\pi}\{K_{te}[\cos\theta_{St} - \cos\theta_{Ex}] + K_{re}[\sin\theta_{St} - \sin\theta_{Ex}]\} \tag{10}$$

where θ_{St} and θ_{Ex} represent the entry and exit angles, respectively. Eqs. (9) and (10) can be arranged in matrix form as

$$\begin{bmatrix} \bar{F}_{x,n} \\ \bar{F}_{y,n} \end{bmatrix} = \boldsymbol{G}_{xy} \begin{bmatrix} K_{tc} \\ K_{te} \\ K_{rc} \\ K_{re} \end{bmatrix} \tag{11}$$

where the subscript n represents the number of cutting conditions for the calibration.

The geometry matrix $\boldsymbol{G}_{xy}$ in Eq. (11) is defined by

$$\boldsymbol{G}_{xy} = \begin{bmatrix} a_{1x,n} f_{z,n} & a_{2x,n} & a_{3x,n} f_{z,n} & a_{4x,n} \\ a_{1y,n} f_{z,n} & a_{2y,n} & a_{3y,n} f_{z,n} & a_{4y,n} \end{bmatrix} \tag{12}$$

The elements of the geometry matrix are given in the equations below. For feed direction, the matrix elements are defined as

$$a_{1x} = \frac{N_f\, d_a}{8\pi} [\cos 2\theta_{St} - \cos 2\theta_{Ex}] \tag{13}$$

$$a_{2x} = \frac{N_f\, d_a}{2\pi} [\sin \theta_{Ex} - \sin \theta_{St}] \tag{14}$$

$$a_{3x} = \frac{N_f\, d_a}{8\pi} [(2\theta_{Ex} - 2\theta_{St}) + (\sin 2\theta_{St} - \sin 2\theta_{Ex})] \tag{15}$$

$$a_{4x} = \frac{N_f\, d_a}{2\pi} [\cos \theta_{St} - \cos \theta_{Ex}] \tag{16}$$

For transverse direction, the matrix elements are defined as

$$a_{1y} = \frac{N_f\, d_a}{8\pi} [(2\theta_{Ex} - 2\theta_{St}) + (\sin 2\theta_{St} - \sin 2\theta_{Ex})] \tag{17}$$

$$a_{2y} = \frac{N_f\, d_a}{2\pi} [\cos \theta_{St} - \cos \theta_{Ex}] \tag{18}$$

$$a_{3y} = \frac{N_f\, d_a}{8\pi} [\cos 2\theta_{Ex} - \cos 2\theta_{St}] \tag{19}$$

$$a_{4y} = \frac{N_f\, d_a}{2\pi} [\sin \theta_{St} - \sin \theta_{Ex}] \tag{20}$$

Applying least-squares fitting method to the force vector and geometry matrix, the coefficients are calibrated as follows

$$\begin{bmatrix} K_{tc} \\ K_{te} \\ K_{rc} \\ K_{re} \end{bmatrix} = \left[\boldsymbol{G}_{xy}^T \boldsymbol{G}_{xy}\right]^{-1} \boldsymbol{G}_{xy}^T \begin{bmatrix} \bar{F}_{x,n} \\ \bar{F}_{y,n} \end{bmatrix} \tag{21}$$

4. Instantaneous CHIP thickness model

There are two types of tool runout, radial and axial. The axial runout, whose influence on the cutting forces is disregarded, is very small compared to the axial depth. However, the radial runout has the same order as feed per tooth (Li and Li 2004). Therefore, the analysis is focused on radial runout, which is described as the offset of tool from the axis of rotation.

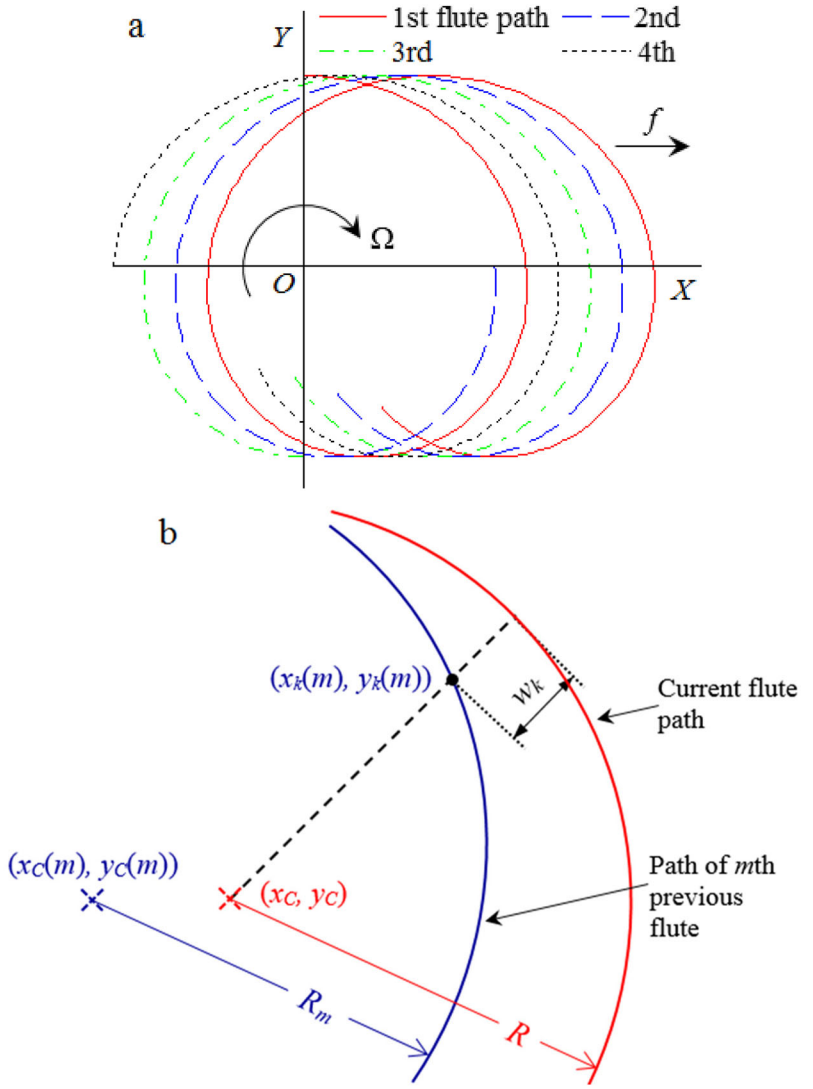

Figure 4. Helical-flute end milling with runout: (**a**) Trochoidal trajectory, (**b**) Chip thickness geometry.

The trajectories of cutting edges with respect to the workpiece in milling are trochoidal (Kumanchik and Schmitz 2007), as illustrated in Fig. 4a. The undeformed chip thickness can be modeled by considering flute trajectories incorporating tool runout (Sutherland and DeVor 1986).

The trajectory of the cutting point at the tip of a flute is given as

$$\begin{aligned} x_k &= R\,\sin\left(\theta_k(t)\right) + x_C \\ y_k &= R\,\cos\left(\theta_k(t)\right) + y_C \end{aligned} \tag{22}$$

The position of the tool center in the coordinate system XOY can also be described as follows

$$\begin{aligned} x_C &= \rho\,\sin\left(\lambda + \phi(j)\right) + ft \\ y_C &= \rho\,\cos\left(\lambda + \phi(j)\right) \end{aligned} \tag{23}$$

where x_C and y_C are the coordinates of tool center in feed and transverse directions, respectively. f is the feed rate. t is the time. ρ is the runout offset, and λ is the location angle. The trochoidal motion, which occurs in feed direction, is accounted for through the expression ft.

The undeformed chip thickness is the difference between the path that the current flute is generating and the workpiece surface left by a previously passing flute. When the tip of the mth previous flute is at the point $(x_k(m), y_k(m))$, the coordinates of this point can be found from Eq. (22). At this moment, the center of tool is at the point $(x_C(m), y_C(m))$, and its coordinates can be obtained using Eq. (23).

Fig. 4b illustrates the intersection of the line depicted by the current flute engagement angle with the surface generated by the mth previous flute. This line can be expressed as

$$y_k(m) = \frac{-1}{\tan(\theta)} x_k(m) \tag{24}$$

The workpiece surface generated by the mth previous flute can be defined as

$$[x_k(m) - x_C(m)]^2 + [y_k(m) - y_C(m)]^2 = R^2 \tag{25}$$

The instantaneous undeformed chip thickness (w_k) can be determined as follows (Sutherland and DeVor 1986)

$$w_k(i,j,k,m) = R - \sqrt{x_k(m)^2 + y_k(m)^2} \tag{26}$$

$$w_k(\theta) = \text{Max}[0, \text{Min}(w_k(i,j,k,m))] \tag{27}$$

5. Determination of runout parameters

The radius of each flute can be measured when the end mill is attached to the spindle. Assuming that on an end mill with clockwise rotation, there are N_f flutes labeled counterclockwise as No. 1, 2, …, N_f, and the flutes are uniformly distributed. By ignoring the runout perpendicular to the cutting edge as shown in Eq. (28), the actual radius of the kth flute can be regarded as $R_k = R + e_{rk}$, where e_{rk} is the runout offset of the kth flute (Yalcin 2009). Fig. 5 shows the convention employed for runout.

$$R_1 = \sqrt{(R + \rho\ \cos\lambda)^2 + \underbrace{(\rho\ \sin\lambda)^2}_{\text{negligible}}} = R + \rho\ \cos\lambda \tag{28}$$

Thus, the radius of each flute for a four-flute end mill can be defined as

$$\left.\begin{aligned} R_1 &= R + \rho\ \cos\lambda = R + e_{r1} \\ R_3 &= R - \rho\ \cos\lambda = R + e_{r3} \end{aligned}\right\} \Rightarrow e_{r1} - e_{r3} = 2\rho\cos\lambda$$
$$\left.\begin{aligned} R_4 &= R + \rho\ \sin\lambda = R + e_{r4} \\ R_2 &= R - \rho\ \sin\lambda = R + e_{r2} \end{aligned}\right\} \Rightarrow e_{r4} - e_{r2} = 2\rho\sin\lambda \tag{29}$$

From the above equations, the runout offset and location angle can be found as

$$\rho = \frac{\sqrt{(e_{r1} - e_{r3})^2 + (e_{r4} - e_{r2})^2}}{2}, \lambda = \tan^{-1}\left[\frac{e_{r4} - e_{r2}}{e_{r1} - e_{r3}}\right] \tag{30}$$

It is noted that the location angle is set to its minimum positive equivalent $0 \leq \lambda < 90^\circ$ for the four-flute end mill.

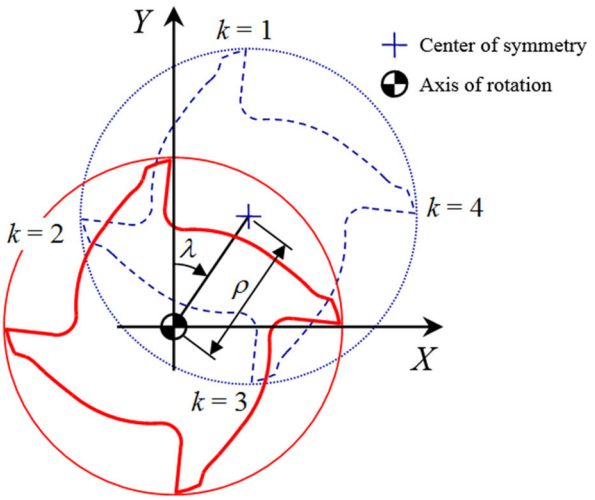

Figure 5. Runout offset and location angle definitions.

6. Milling experiment procedure

In this section, the experimental procedure of flat-end milling process has been presented in detail. As can be seen in the following, the radii of all flutes at the free end of the end mill were measured to identify the tool runout parameters, and the cutting force measurements were carried out.

6.1. Milling machine

The entire milling experiments were performed on 3-axis Quaser MV154C vertical milling machine. It has a maximum spindle speed of 10,000 rev/min. The machine table moves in feed and transverse directions, and the spindle moves vertically on the column.

6.2. Experimental setup

The cutting forces were measured by using a standard quartz dynamometer (Kistler 9257B) which was fixed on the machine table. The dynamometer was connected to the computer through a charge amplifier (Kistler 5070) and National Instruments data acquisition card. Post-processing of data was treated through DynoWare software. Before the cutting experiments, the tool runout was adjusted by placing a thin aluminum alloy film with the end mill in the tool chuck. Then, the radii of all flutes at the free ends of the end mills were measured through a dial indicator with a precision of 0.001 mm to quantify the runout values for each cutting tool. To minimize the influence of runout measurement deviations, each measurement was repeated two times to establish a statistical mean. Table 1 lists the calculated runout parameters for each tool. Fig. 6 shows the experimental setups for cutting force and tool runout measurements.

6.3. Cutting tools

The cutting tools were uncoated tungsten carbide flat-end mills with 12 mm diameter held in a tool holder mounted on the spindle, which had either straight or helical flutes. The helix angle for helical-flute tools was 30°. For calibration, experiments were performed with single-flute tools

Table 1. Runout parameters.

Tool	Runout offset, ρ (mm)	Location angle, λ (°)
Straight-flute	5.06×10^{-3}	69.9
Helical-flute	5.22×10^{-3}	73.3

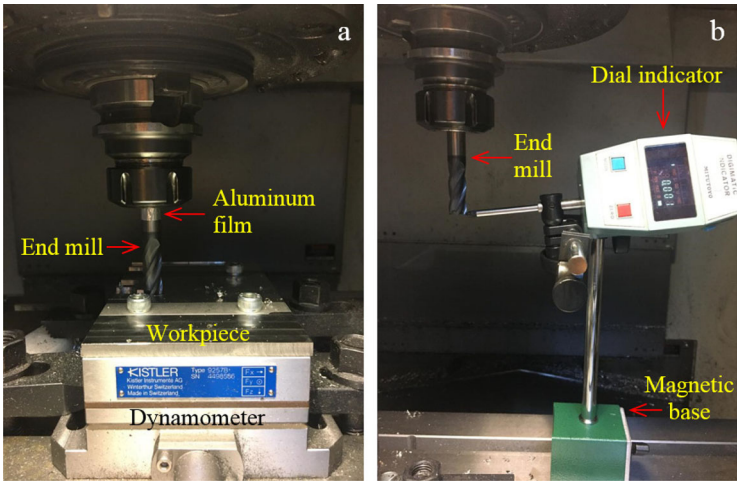

Figure 6. Experimental setups: (**a**) Cutting force measurement, (**b**) Runout measurement.

to simplify the experimental work. Then, four-flute ones were used to investigate the effects of tool engagement, tool geometry and workpiece material. The cutting tools are shown in Fig. 7.

6.4. Workpiece materials

Cutting forces were analyzed under dry machining for two different workpiece materials with high strength: AZ31 Mg-alloy and Ti6Al4V alloy. All the machined specimens had dimensions of $170 \times 100 \times 12$ mm, which were rigidly clamped on the dynamometer. The workpiece was fed toward the tool so that there was a relative movement between the rotating tool and workpiece during experiments.

6.5. Cutting conditions

An extensive range of spindle speeds in conventional-speed milling process was considered to obtain completely data about machinability of AZ31 Mg-alloy and Ti6Al4V alloy with the straight and helical-flute end mills. To evaluate the effect of spindle speed on the force coefficients, three sets of calibration experiments were performed with three different spindle speeds of 600, 1200 and 3000 rev/min. For each set, four different feed rates were tested by changing the feed per tooth (f_z) from 0.025 to 0.1 mm/flute in steps of 0.025 mm/flute while other parameters constant. Table 2 depicts the experimental design for calculating the force coefficients.

In addition to calibration experiments, cutting experiments were performed to evaluate the effects of tool engagement, tool geometry and workpiece material on cutting forces using straight and helical-flute end mills with four flutes. It was focused on slot cutting and shoulder milling in down and up cutting configurations to study different tool engagement conditions. The tool engagement was defined with a radial depth (d_r) of 6 mm for shoulder milling. The axial depth (d_a) was kept constant at 2 mm for the entire experiments.

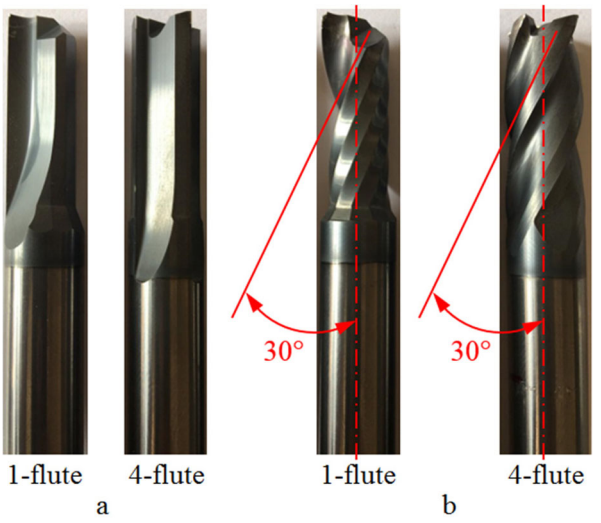

Figure 7. Cutting tools: (**a**) Straight-flute, (**b**) Helical-flute.

Table 2. Experimental design used in calibration of force coefficients.

	Forces at different feeds per tooth for each tool-workpiece combination					
	AZ31 Mg-alloy				Ti6Al4V alloy	
Feed per tooth (mm/flute)	Straight-flute end mill		Helical-flute end mill		Helical-flute end mill	
0.025	$F_{x,1}$	$F_{y,1}$	$F_{x,1}$	$F_{y,1}$	$F_{x,1}$	$F_{y,1}$
…	…	…	…	…	…	…
…	…	…	…	…	…	…
…	…	…	…	…	…	…
0.1	$F_{x,4}$	$F_{y,4}$	$F_{x,4}$	$F_{y,4}$	$F_{x,4}$	$F_{y,4}$

7. Results and discussion

This section considers the effects of tool geometry, workpiece material and cutting parameters such as spindle speed, tool engagement and cutting direction on the cutting forces. Moreover, the force coefficients and the cutting forces obtained mechanistically are presented for different tool/workpiece pairs. The effect of tool runout on the instantaneous forces is discussed.

7.1. Force coefficients for different tool/workpiece materials

All the cutting force curves obtained from milling experiments have the characteristic shape presented in Fig. 8a. Unstable regions appear at the beginning and end of the curves, corresponding to entry and exit of the tool. To calibrate the force coefficients, average cutting forces were calculated from graphical data obtained in the steady-state region at the center of the curves for 10 spindle revolutions, as given in Fig. 8b.

To analyze the influence of workpiece material on the force coefficients, average cutting forces in feed and transverse directions were obtained using a single-flute helical end mill for two types of workpiece materials: AZ31 Mg-alloy and Ti6Al4V alloy. Fig. 9 shows the relationship between feeds per tooth and average cutting forces for carbide/AZ31 Mg-alloy pair. It can be observed that the average cutting forces change linearly with the feed per tooth. Besides, when the spindle speed increases from 600 to 3000 rev/min, these linear relationships have the similar gradient.

The relationship between feeds per tooth and average cutting forces for carbide/Ti6Al4V alloy pair is illustrated in Fig. 10. As reported by other researchers (Rubeo and Schmitz 2016), the

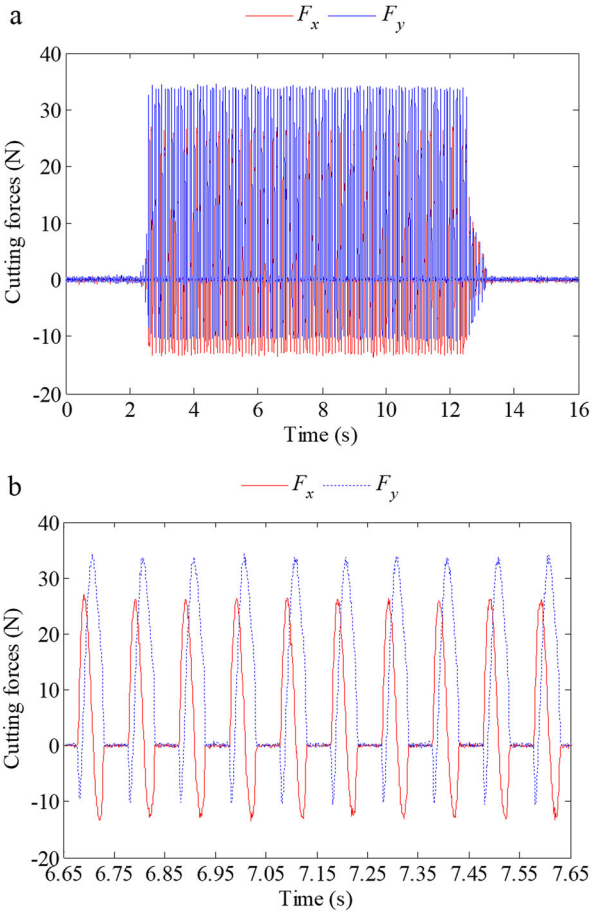

Figure 8. Cutting forces measured in slot cutting with helical-flute end mill (Workpiece: AZ31 Mg-alloy, $\Omega = 600$rev/min, $f_z = 0.025$mm/flute, $d_a = 2$mm): (**a**) Global cutting forces, (**b**) 10 periods of cutting forces in steady-state region.

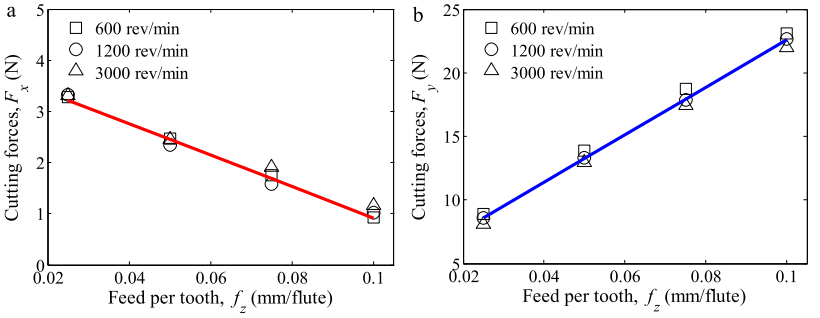

Figure 9. Variation of average cutting forces with feed per tooth at different spindle speeds for helical-flute carbide end mill/AZ31 Mg-alloy: (**a**) Feed force, (**b**) Transverse force.

average cutting forces increase linearly as the feed per tooth increases, and the gradients of the linear relationships of average cutting forces in feed and transverse directions vary with increasing spindle speed. In addition, the magnitudes of the feed and transverse forces decrease as the spindle speed increases.

The cutting and edge force coefficients calibrated from the least-squares method by using the average forces for two different tool/workpiece pairs are listed in Table 3. As can be seen, the

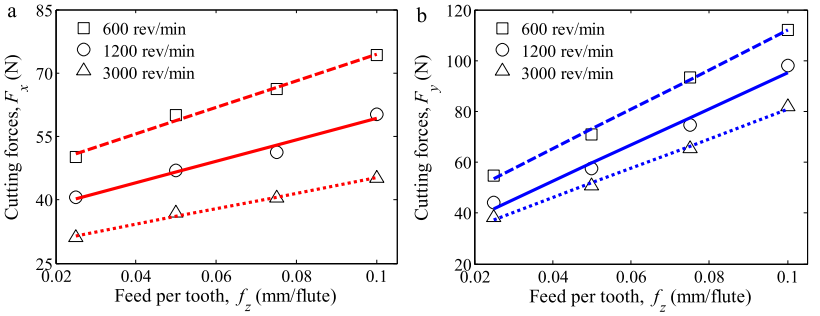

Figure 10. Variation of average cutting forces with feed per tooth at different spindle speeds for helical-flute carbide end mill/Ti6Al4V alloy: (**a**) Feed force, (**b**) Transverse force.

Table 3. Calibrated force coefficients for different tool/workpiece combinations.

Spindle speed, Ω (rev/min)	Tool	Workpiece	K_{tc} (N/mm^2)	K_{te} (N/mm)	K_{rc} (N/mm^2)	K_{re} (N/mm)
600	Carbide helical-flute end mill	AZ31 Mg	378.69	6.77	−62.27	6.37
		Ti6Al4V	1553.86	53.78	625.91	67.73
1200		AZ31 Mg	374.13	6.16	−61.27	6.25
		Ti6Al4V	1427.42	37.69	505.67	53.4
3000		AZ31 Mg	369.67	5.62	−55.81	6.21
		Ti6Al4V	1162.13	35.74	364.72	42.4

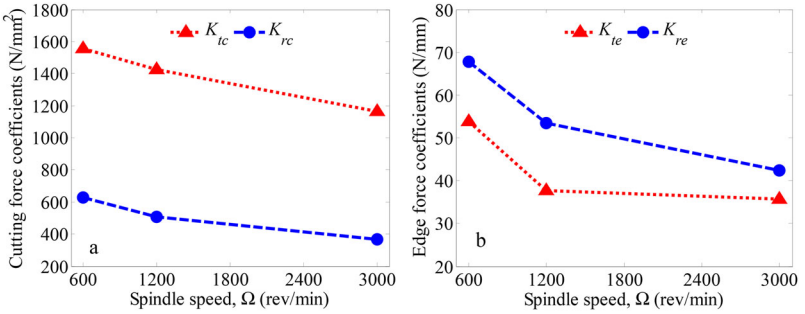

Figure 11. Calibrated force coefficients versus spindle speeds in machining Ti6Al4V alloy: (**a**) Cutting force coefficients, (**b**) Edge force coefficients.

force coefficients for each tool/workpiece combination vary when cutting with the same milling parameters. The tangential and radial cutting force coefficients calculated when machining Ti6Al4V alloy are higher than those obtained in cutting AZ31 Mg-alloy. Further, it is found that when the speed is changed from 600 to 3000 rev/min, the tangential and radial cutting force coefficients decrease slightly by 2.44 and 11.57% for AZ31-Mg alloy, respectively. However, there is a larger decrease of 33.71 and 71.61% in tangential and radial cutting force coefficients for Ti6Al4V alloy, respectively. These phenomena reveal that the cutting force coefficients calculated for AZ31-Mg alloy are not very sensitive to the variation of spindle speed. However, due to the variation of shearing behavior during cutting Ti6Al4V alloy at different spindle speeds, the cutting force coefficients depend upon the speed as seen in Fig. 11a. Also, the resulting trend is in agreement with results in reference (Grossi et al. 2015).

It is well known that the edge force mainly results from the plowing mechanism at the cutting edge, which is associated with the elastic-plastic property of workpiece material (Wan et al. 2016). For AZ31 Mg-alloy, there is no significant difference in tangential and radial edge force coefficients with an increase in spindle speed. On the other hand, as can be also observed in Fig. 11b, there is a decrease of 50.48 and 59.74% in tangential and radial edge force coefficients with

Table 4. Cutting and edge force coefficients for straight and helical-flute end mills.

Spindle speed, Ω (rev/min)	Tool	Workpiece	K_{tc} (N/mm^2)	K_{te} (N/mm)	K_{rc} (N/mm^2)	K_{re} (N/mm)
600	Straight-flute	AZ31 Mg-alloy	444.4	7.66	76.52	11.91
	Helical-flute		378.69	6.77	−62.27	6.37
1200	Straight-flute		435.71	6.3	74.87	7.49
	Helical-flute		374.13	6.16	−61.27	6.25
3000	Straight-flute		420.98	5.33	69.66	5.71
	Helical-flute		369.67	5.62	−55.81	6.21

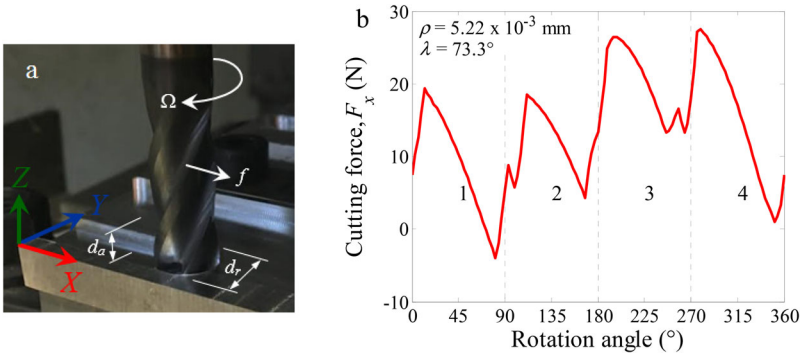

Figure 12. Slot cutting configuration: (**a**) Tool engagement, (**b**) Theoretical cutting force curve.

increasing spindle speed from 600 to 3000 rev/min for Ti6Al4V alloy, respectively. Consequently, the edge force coefficients are noticeably dependent on the properties of workpiece materials. The decrease in coefficients can be also associated with the softening of the workpiece material because of the tool-chip interface temperature increasing with spindle speed.

7.2. Force coefficients for cutting tools with different helix angle

To identify the force coefficients for end mills with straight and helical flutes, the average cutting forces in feed and transverse directions were obtained under different spindle speeds during milling of AZ31 Mg-alloy.

The calibrated cutting and edge force coefficients are listed in Table 4. It is found that when the spindle speed is changed from 600 to 3000 rev/min, the tangential cutting force coefficients decrease by 5.56 and 2.44% for straight and helical-flute end mills, respectively. Moreover, a comparison of radial cutting force coefficients reveals that there is a decrease of 9.85 and 11.57% with increasing spindle speed from 600 to 3000 rev/min for straight and helical-flute tools, respectively. It is evident from the above results that the magnitudes of the tangential and radial cutting force coefficients are influenced from the variation of the spindle speed. Accordingly, these coefficients can be determined as constant values with respect to the variation of spindle speed.

By comparing the cutting force coefficients, it can be also seen that the cutting coefficients determined using straight-flute end mill are higher than those obtained by the helical tool. It is noteworthy here that increasing helix angle serves to decrease the cutting force coefficients. For the tangential and radial edge force coefficients, it is observed a slight variation when using cutting tools with different helix angle or different spindle speeds. It can be concluded that the edge coefficients are quite independent of tool geometry.

7.3. Tool engagement conditions in milling

To more carefully investigate the effect of runout on the instantaneous force profile within the envelope, the tool engagement conditions including slot cutting and shoulder milling in down

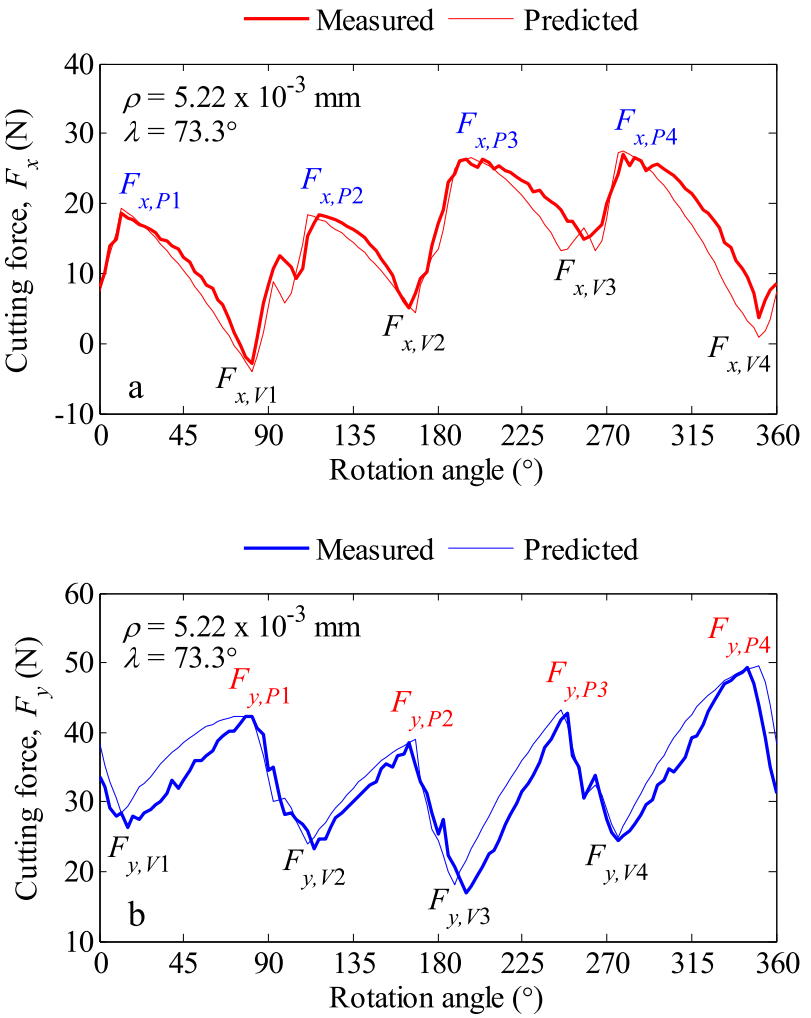

Figure 13. Measured and predicted force curves in slot cutting: (**a**) Feed force, (**b**) Transverse force ($\Omega = 600$ rev/min, $f_z = 0.025$ mm/flute, $d_a = 2$ mm).

and up cutting configurations were analyzed for conventional-speed milling. The cutting tool was a four-flute helical end mill. The workpiece material was AZ31 Mg-alloy.

Fig. 12 illustrates the slot cutting configuration and the cutting force curve in feed direction with considering the tool runout obtained mechanistically at the spindle speed of 600 rev/min and feed per tooth of 0.025 mm/flute. It can be observed that the force curve has different peak values in one revolution of the tool since the runout causes each flute to experience a different chip thickness. Besides, its peaks and shape are easily identifiable. Thus, the predicted feed force was adopted to analyze cutting force curves. For four-flute $k = 1, 2, 3, 4$, the mean radial runouts (e_{rk}) are -0.008, -0.0055, 0.002, -0.0025 mm, respectively. The difference of the radius of the actual kth flute with respect to the previous $(k+1)$th one is denoted as $\delta e_{rk} = e_{rk} - e_{rk+1}$. In this case, δe_{rk} is -0.0025, -0.0075, 0.0045, -0.0055 mm for $k = 1, 2, 3, 4$, respectively. Since the absolute radius variation for a flute with respect to the previous one is smaller than the feed per tooth, i.e., $|\delta e_{rk}| < f_z$, every flute engages in cutting.

To reveal the presence of runout, four stages are considered as a function of the cutting tool rotation angle, corresponding to the entry and exit cut of the four flutes. Each one describes a characteristic evolution of the cutting force curve: Slot cutting begins when the initial flute

Table 5. Comparison of measured and predicted average force amplitudes for slot cutting $f_z = 0.025$ mm/flute, $d_a = 2$ mm).

	Feed force (N)			Transverse force (N)			
Spindle speed, Ω (rev/min)	$\bar{F}_x^M$	$\bar{F}_x^E$	$(\bar{F}_x^M - \bar{F}_x^E)^2$	$\bar{F}_y^M$	$\bar{F}_y^E$	$(\bar{F}_y^M - \bar{F}_y^E)^2$	MSE_{tot}
600	19.3	17.3	4	19.7	17.5	4.84	
1200	17.7	15.5	4.84	19.3	16.6	7.29	
3000	16.3	13.7	6.76	19.1	15.1	16	
	MSEx		5.2	MSEy		9.38	14.58

gradually engages in cutting. A unique force peak occurs and the force decreases quickly to valley value. During the second stage, the cut geometry makes the force peak slightly different. In the third stage of slot cutting, the curve immediately begins another identical cycle but a higher force peak is produced. It is clear that this step corresponds to the entry of the high side of the tool into the workpiece. It can be also concluded that when the tool enters the cut, its low side is engaged with the workpiece. The fourth stage corresponding to the end of the cutting cycle produces a slightly higher force peak but lower force valley compared with the third stage. As a result, the magnitude of force peak becomes different at each stage since the chip load for each flute varies due to the presence of runout.

In case of slot cutting, the comparisons of cutting force curves obtained from the experiment and predicted from the time domain simulation are also presented in Fig. 13. It can be observed that the shape and amplitudes of the predicted cutting force profiles are in good agreement with the measured ones. Due to the existence of tool runout, the amplitudes of the measured and predicted cutting forces vary with the cutting tool rotation. The flutes on the high side of the tool are engaged with the workpiece more than those on its low side, and cause higher cutting force peaks. The differences of feed and transverse force peaks between the low and high sides of cutting tool are ratios of about 50 and 25%, respectively.

For a better comparison of the results obtained from the mechanistic model, the varying amplitudes of feed and transverse force curves are analyzed, and the average of the cutting force amplitudes is obtained considering two successive revolutions, i.e., eight peaks and valleys in the curves. The peaks ($F_{x,P1}$, …, $F_{x,P4}$) and valleys ($F_{x,V1}$, …, $F_{x,V4}$) for one tool revolution are marked in Fig. 13. The average amplitude is calculated as given below

$$\bar{F}_q = \left| \frac{(F_{q,P1} + F_{q,P2} + F_{q,P3} + \ldots + F_{q,P8}) - (F_{q,V1} + F_{q,V2} + F_{q,V3} + \ldots + F_{q,V8})}{8} \right| (q = x, y) \quad (31)$$

In this study, the mean squared errors of average amplitudes (MSE) are taken as a measure of performance of the mechanistic model, and calculated as follows

$$MSE_q = \frac{1}{n_s} \sum_{\Omega=600}^{3000} (\bar{F}_q^M - \bar{F}_q^E)^2 (q = x, y) \quad (32)$$

where $\bar{F}_q^M$ and $\bar{F}_q^E$ are the average amplitudes of the predicted and measured signals at each spindle speed, respectively, n_s is the number of spindle speeds ($n_s = 3$). The total of the mean squared errors (MSE_{tot}) for feed and transverse forces is computed as

$$MSE_{tot} = MSE_x + MSE_y \quad (33)$$

Table 5 lists the average amplitudes along with the squared errors for the feed and transverse forces. Comparing the prediction errors, it is seen that the squared errors increase as the spindle speed increases in slot cutting conditions with the same axial depth and feed per tooth. The best correlation is achieved under low spindle speed. The force model performs well for the feed force with a mean squared error of 5.2 while a slightly higher prediction error of 9.38 is calculated for transverse force. The total of the mean squared errors is also found as 14.58.

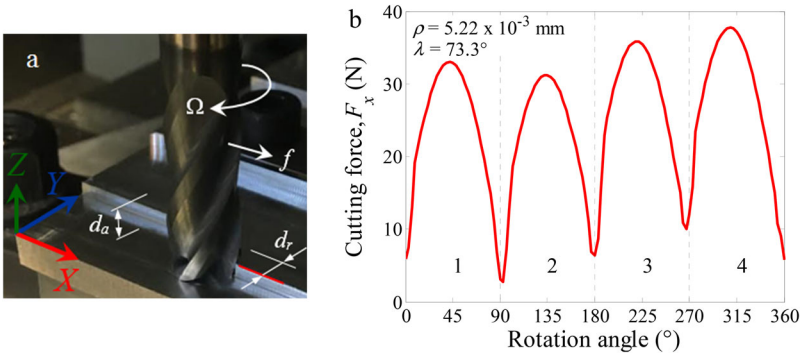

Figure 14. Up cutting configuration: (**a**) Tool engagement, (**b**) Theoretical cutting force curve.

Up cutting configuration is illustrated in Fig. 14a, which corresponds to a radial immersion of 50%. Fig. 14b plots the predicted cutting force curve at the spindle speed of 600 rev/min and feed per tooth of 0.05 mm/flute, and four main stages are described: Up cutting begins with a chip thickness equal to zero. As the tool rotates, the cutting force gradually increases and a force peak occurs. At the end of the cut, the chip is removed, and the initial flute comes out of the workpiece. In the second stage, a slightly varying force peak and valley reveal compared with the first stage. In the third stage, the force peak is greater than those in the preceding stages. This means the entry of the high side of the tool into the workpiece. Many phenomena such as wear, vibration can occur due to increasing chip load. The fourth stage corresponds the largest force peak. It should be noted here that there are nickpoints on the curve, which correspond to the quickly entry of the flutes into the workpiece.

For the case of up cutting that is illustrated in Fig. 15, the mechanistic model gives a good description of feed and transverse forces with slight deviations in the peak and valley regions. The cutting force curves indicate a behavior close to sinusoidal, and the tool runout vary the distribution of cutting forces between each flute of the cutting tool. Also, it can be observed from the curves that the cutting process is continuous.

It is interesting to compare the average amplitudes of the experimental cutting forces with those calculated mechanistically for three different spindle speeds. For up milling, Table 6 presents the average amplitudes. The mean squared errors are found as 17.53 and 65.35 for feed and transverse forces, respectively. The total of the mean squared errors is as high as 82.88. There is a lower accuracy for the forces derived from the mechanistic model with the rigid tool assumption at the higher spindle speed. Thus, the vibration phenomenon and flexible behavior of the tool should be considered when modeling the cutting forces at higher spindle speeds.

Down cutting configuration with a radial immersion of 50% and the cutting force curve predicted at spindle speed of 600 rev/min and feed per tooth of 0.075 mm/flute are shown in Fig. 16. Down cutting begins with the entry of the initial flute from the straight workpiece surface. Negative magnitudes are observed in the curve because of mainly the projection of forces on the relief surface of the tool (Maurel-Pantel et al. 2013), which coincide with the findings of Kline and DeVor (1983). In the second stage, the tool produces a slightly lower force peak than the first stage. The third stage occurs a higher force peak than the other stages due to the entry of the high side of the tool into the workpiece. The nickpoint on the curve indicates that the cutting force increases quickly in the positive direction. The fourth stage is characterized by the largest negative value, and is a critical place for the cutting force.

In the down cutting case, the experimentally observed force curves and the predicted force curves are presented in Fig. 17. It can be observed that the model is able to predict the variations of cutting forces with rotation angle while small deviations are available in the peak and valley

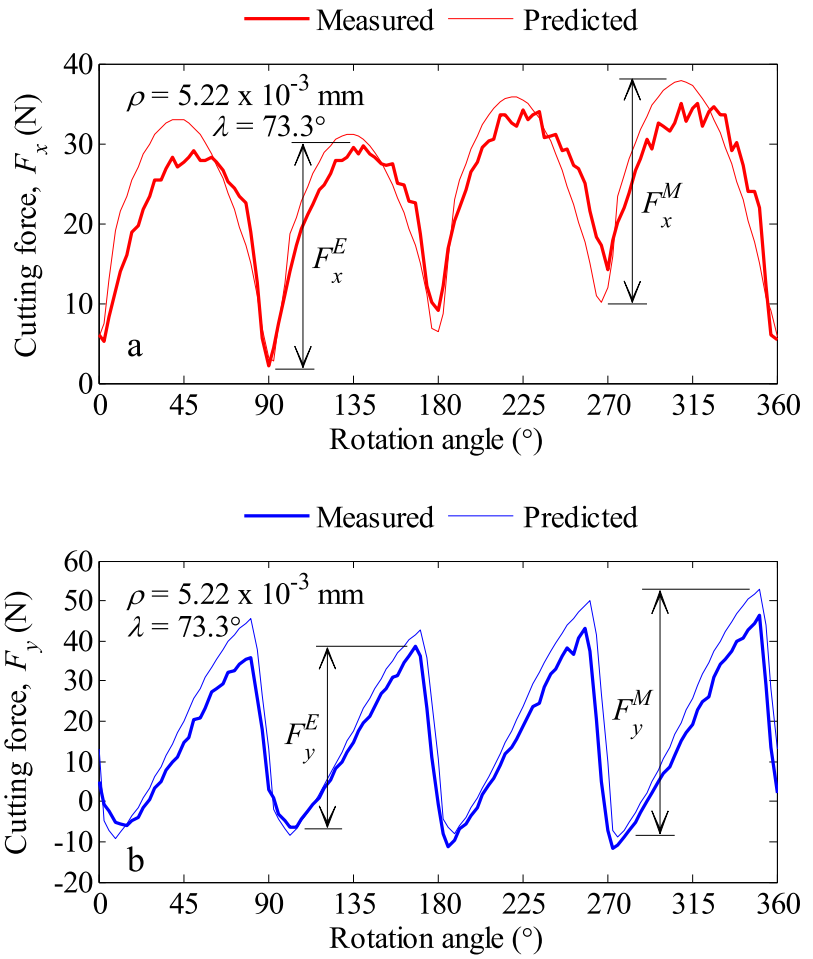

Figure 15. Measured and predicted force curves in up cutting: (**a**) Feed force, (**b**) Transverse force ($\Omega = 600$rev/min, $f_z = 0.05$ mm/flute, $d_a = 2$ mm).

Table 6. Comparison of measured and predicted average force amplitudes for up cutting ($f_z = 0.05$ mm/flute, $d_a = 2$ mm).

	Feed force (N)			Transverse force (N)			
Spindle speed, Ω (rev/min)	$\bar{F}_x^M$	$\bar{F}_x^E$	$(\bar{F}_x^M - \bar{F}_x^E)^2$	$\bar{F}_y^M$	$\bar{F}_y^E$	$(\bar{F}_y^M - \bar{F}_y^E)^2$	MSE_{tot}
600	29.4	25.7	13.69	56.5	50.4	37.21	
1200	28.4	24.3	16.81	54.9	47.1	60.84	
3000	27.7	23	22.09	53.5	43.6	98.01	
	MSEx		17.53	MSEy		65.35	82.88

regions of cutting force curves. In case of four-flute, each flute path has its own profile shape and magnitude in one tool revolution since the tool runout exists. The variations in the forces are symmetric to those in up cutting.

In order to compute the deviation between the force amplitudes for down cutting configuration with runout, the experimentally measured force amplitudes and the amplitudes derived from the mechanistic force model are presented in Table 7. The predicted feed force from the force model integrated with the chip thickness model has a mean squared error of 27.71 while the prediction error is high up to 52.59 for transverse force. Further, the total of the mean squared errors is calculated as 80.3. A better accuracy is obtained under the condition with lower spindle speed.

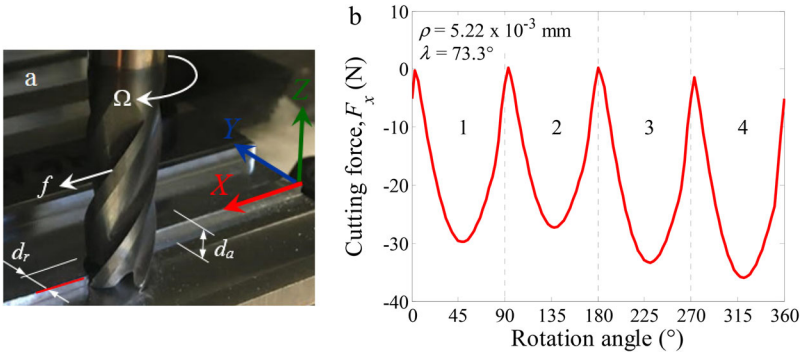

Figure 16. Down cutting configuration: (**a**) Tool engagement, (**b**) Theoretical cutting force curve.

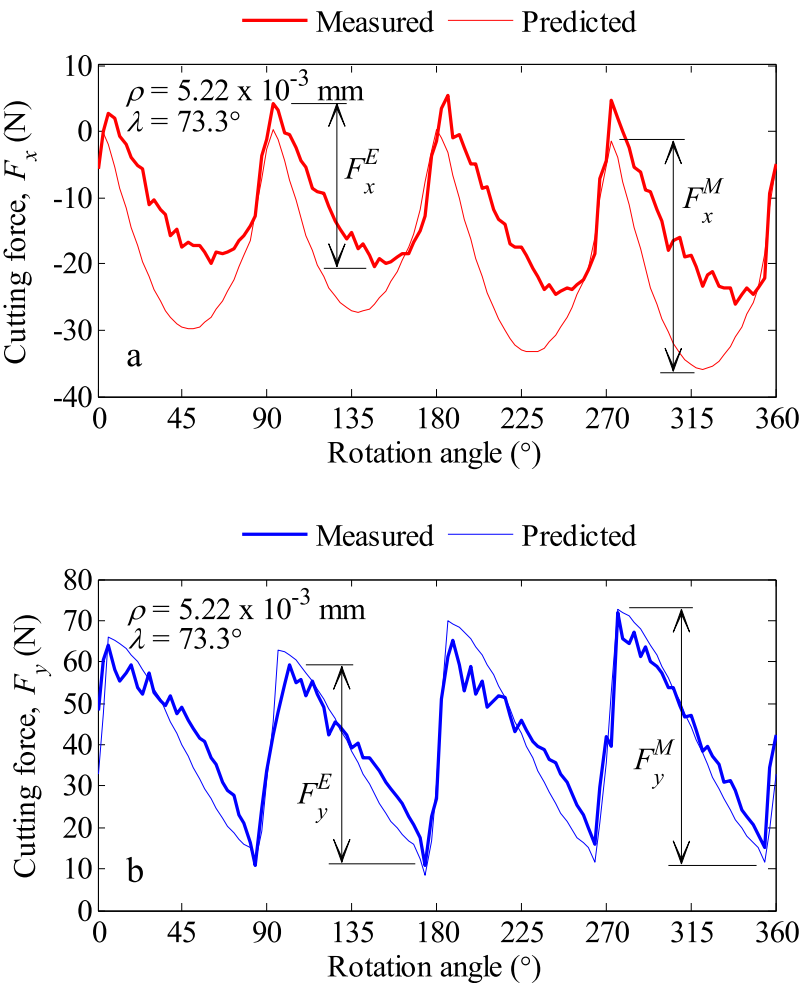

Figure 17. Measured and predicted force curves in down cutting: (**a**) Feed force, (**b**) Transverse force ($\Omega = 600$rev/min, $f_z = 0.075$ mm/flute, $d_a = 2$ mm).

As presented above, the accuracy of force predictions is sensitive to the tool engagement condition. The predicted cutting forces are more accurate in the slot cutting configuration for the tested cutting speed range. For the cases of up and down cutting, the feed and transverse forces are predicted with a lower accuracy.

Table 7. Comparison of measured and predicted average force amplitudes for down cutting ($f_z = 0.075$ mm/flute, $d_a = 2$ mm).

	Feed force (N)			Transverse force (N)			
Spindle speed, Ω (rev/min)	$\bar{F}_x^M$	$\bar{F}_x^E$	$(\bar{F}_x^M - \bar{F}_x^E)^2$	$\bar{F}_y^M$	$\bar{F}_y^E$	$(\bar{F}_y^M - \bar{F}_y^E)^2$	MSE_{tot}
600	30.9	26.7	17.64	57	51.6	29.16	
1200	29.8	24.6	27.04	55.5	48.6	47.61	
3000	29	22.8	38.44	53.9	44.9	81	
	MSEx		27.71	MSEy		52.59	80.3

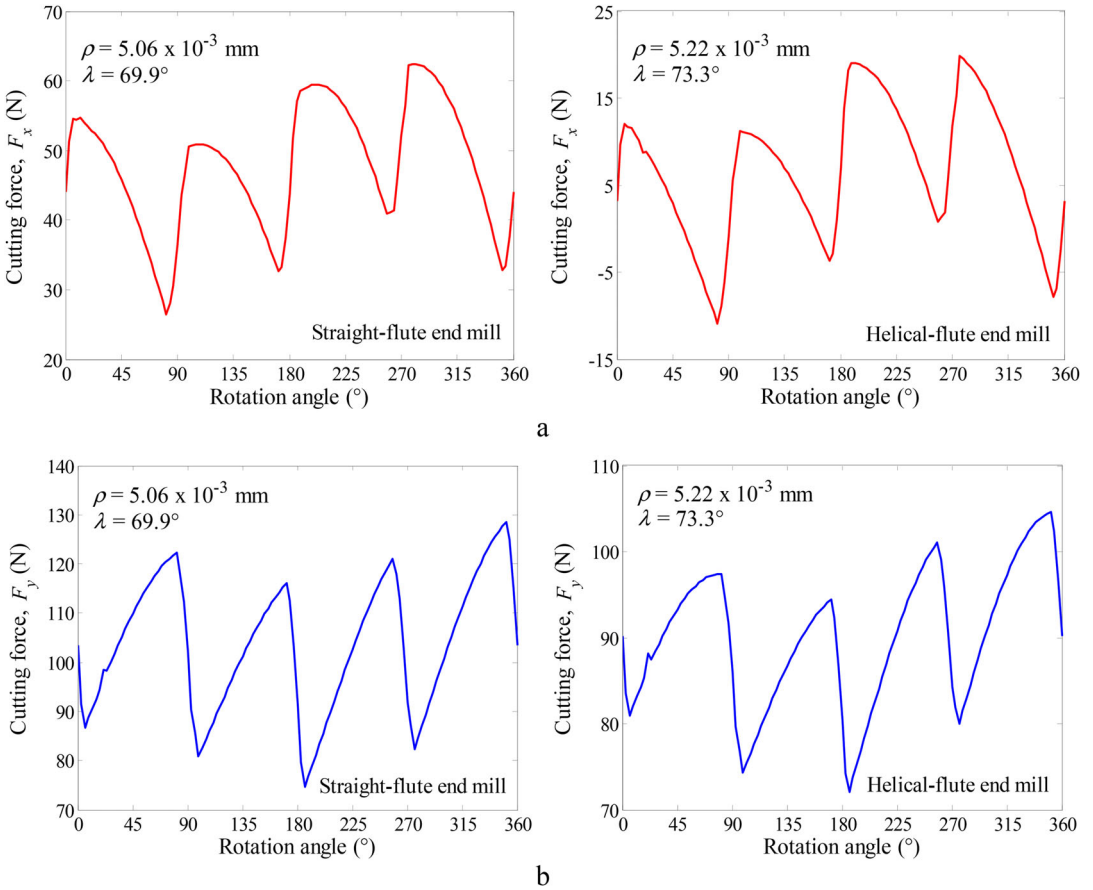

Figure 18. Cutting force curves predicted using straight and helical-flute end mills: (**a**) Feed force, (**b**) Transverse force ($\Omega = 600$rev/min, $f_z = 0.1$ mm/flute, $d_a = 2$ mm).

7.4. Influence of different tool geometries on cutting forces

To study the influences of tool geometries on cutting forces for milling process with runout, the straight and helical end mills having four flutes were analyzed at constant feed per tooth of 0.1 mm/flute for a wide range of speeds, namely 600, 1200 and 3000 rev/min. For each spindle speed, slot cutting processes were performed on AZ31 Mg-alloy.

As can be seen from the predicted force curves in Fig. 18, the straight-flute end mill gives greater force peaks than helical-flute tool at the spindle speed of 600 rev/min. There is a sharper transition at the peak regions of feed force for end mill that has helical flutes compared with straight-flute end mill. On the other hand, a smoother transition is observed at peak regions of feed force for straight-flute end mill. For transverse forces, both straight and helical-flute end mills exhibit a sharp transition at the peak regions of each flute pass period.

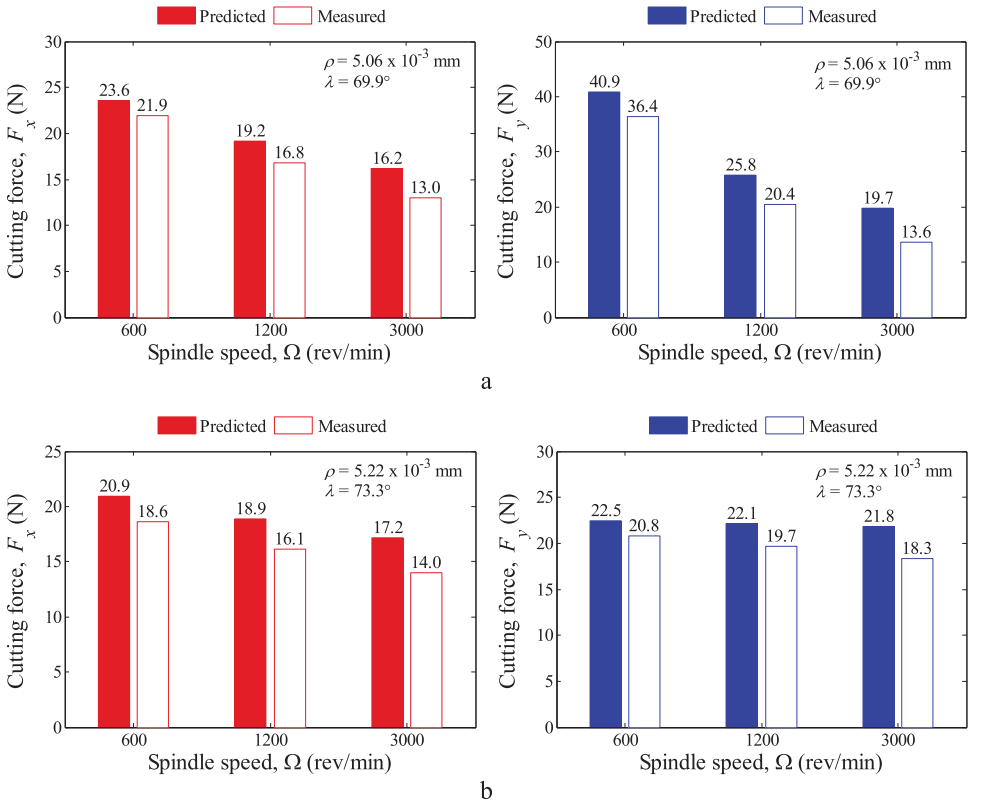

Figure 19. Measured and predicted cutting forces using straight and helical-flute end mills: (**a**) Straight-flute, (**b**) Helical-flute ($f_z = 0.1$ mm/flute, $d_a = 2$ mm).

Fig. 19 shows the effects of runout on the average cutting force amplitudes for two different end mills with straight and helical flutes. It can be observed that the mechanistic model overestimates the force values consistently in the spindle speed range compared with experimental observations. This can be associated with the fact that tool wear is not considered in the model. The amplitudes of the measured and predicted feed and transverse forces tend to decrease as the spindle speed increases, which can be explained by the following: (i) It is generally observed that a decrease in spindle speed decreases the shear angle, and a small shear angle gives a large shear-plane area. Thus, the shear forces needed for deformation increase; (ii) At low spindle speed, the cutting forces increase due to high friction coefficient. At the spindle speed of 600 rev/min, the helical-flute end mill leads to a relatively small decrease of the feed force compared with the straight-flute tool. However, the measured and predicted transverse forces by the helical-flute end mill are considerably lower than those obtained using straight-flute tool at the same spindle speed. From these explanations, it is clearly seen that helical-flute end mill greatly decreases the transverse force at low speed. For the spindle speed of 3000 rev/min, the feed and transverse forces increase slightly with the helix angle.

In addition, the prediction errors for straight and helical-flute end mills are presented in Table 8. The prediction errors in feed and transverse forces for helical-flute end mill are 7.79 and 6.97, respectively. The prediction error in feed force is identified as 6.3 in the case of straight-flute end mill, but the prediction error in transverse force is as high as 28.87. For these tools, the errors of the predicted cutting forces in feed direction are similar. However, the helical-flute end mill provides more accurate predictions for transverse force in contrast to the straight-flute tool. It is obvious that for the case of helical-flute end mill, the mechanistic force model can predict the cutting forces in both feed and transverse direction with a better accuracy.

Table 8. Predicted errors for straight and helical-flute end mills ($f_z = 0.1$ mm/flute, $d_a = 2$ mm).

		Feed force (N)			Transverse force (N)			
Tool	Spindle speed, Ω (rev/min)	$\bar{F}_x^M$	$\bar{F}_x^E$	$(\bar{F}_x^M - \bar{F}_x^E)^2$	$\bar{F}_y^M$	$\bar{F}_y^E$	$(\bar{F}_y^M - \bar{F}_y^E)^2$	MSEtot
Straight-flute	600	23.6	21.9	2.89	40.9	36.4	20.25	
	1200	19.2	16.8	5.76	25.8	20.4	29.16	
	3000	16.2	13	10.24	19.7	13.6	37.21	
		MSE_x		6.3	MSE_y		28.87	35.17
Helical-flute	600	20.9	18.6	5.29	22.5	20.8	2.89	
	1200	18.9	16.1	7.84	22.1	19.7	5.76	
	3000	17.2	14	10.24	21.8	18.3	12.25	
		MSE_x		7.79	MSE_y		6.97	14.76

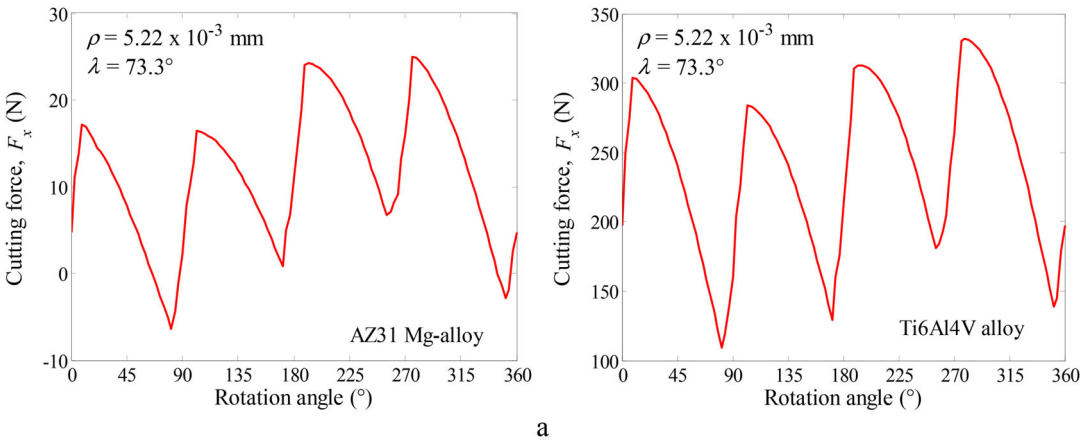

Figure 20. Cutting force curves predicted for AZ31 Mg and Ti6Al4V alloys: (**a**) Feed force, (**b**) Transverse force (Ω = 600 rev/min, $f_z = 0.05$ mm/flute, $d_a = 2$ mm).

7.5. Influence of different workpiece materials on cutting forces

To reveal the influences of workpiece materials on cutting forces for conventional-speed milling process with runout, two different workpiece materials were considered, AZ31 Mg and Ti6Al4V alloys. Slot cutting processes were performed at three different spindle speeds of 600, 1200 and 3000 rev/min with constant feed per tooth of 0.05 mm/flute using four-flute helical end mill.

Based on the force coefficients identified at the spindle speed of 600 rev/min for two different workpiece materials, the predicted cutting force curves are shown in Fig. 20. Ti6Al4V alloy gives

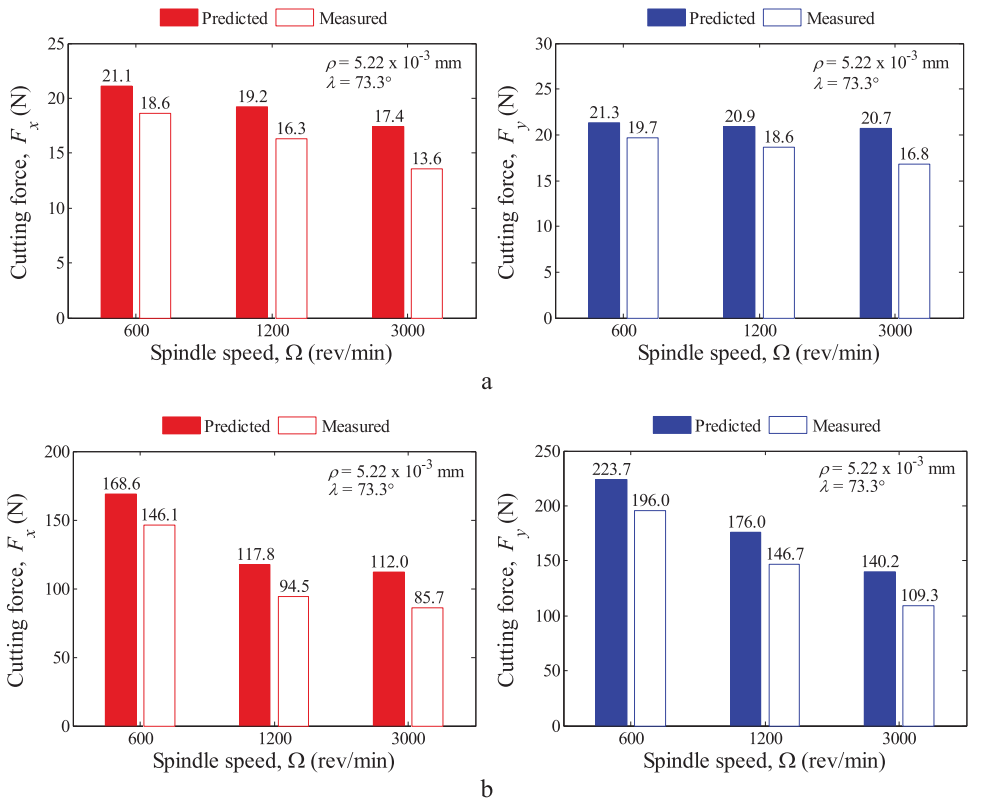

Figure 21. Measured and predicted cutting forces for AZ31 Mg and Ti6Al4V alloys: (**a**) AZ31 Mg-alloy, (**b**) Ti6Al4V alloy ($f_z = 0.05$ mm/flute, $d_a = 2$mm).

substantially greater force amplitudes than AZ31 Mg-alloy under the same cutting condition. From this result, it can be found that the machinability of Ti6Al4V alloy seems to be more critical because of the high value of amplitudes compared with AZ31 Mg-alloy. This phenomenon can be very important in high-speed cutting owing to the dynamic effects appearing with the increase of spindle speed.

Fig. 21 presents the trends of the measured and predicted cutting force amplitudes changing with spindle speed in machining of AZ31 Mg-alloy and Ti6Al4V alloy. It can be observed that the amplitudes of the measured and predicted cutting force components in feed and transverse directions for Ti6Al4V alloy are higher at the spindle speed of 600 rev/min, and show a decrease with increasing spindle speed. Also, AZ31 Mg-alloy results in slightly varying amplitudes with spindle speed. In the case of slot cutting of Ti6Al4V alloy, the measured and predicted feed and transverse forces are considerably higher than those predicted in slot milling of AZ31 Mg-alloy over the spindle speed range.

Table 9 gives the prediction errors for AZ31 Mg and Ti6Al4V alloys. As can be seen from the table, the prediction accuracy of feed and transverse forces is dependent on the workpiece material. In machining of AZ31 Mg-alloy, the prediction errors in feed and transverse forces are 9.7 and 7.69, respectively. The prediction error in feed force is identified as 580.28 in machining of Ti6Al4V alloy; moreover, the error in transverse force prediction is as high as 860.2. That is, Ti6Al4V alloy results in more accurate predictions for feed force in contrast to the transverse force. Finally, it appears that for machining case of AZ31 Mg-alloy, the mechanistic model including the effect of runout can predict the cutting forces with a better accuracy.

Table 9. Predicted errors for AZ31 Mg and Ti6Al4V alloys ($f_z = 0.05$ mm/flute, $d_a = 2$ mm).

Workpiece	Spindle speed, Ω (rev/min)	Feed force (N)			Transverse force (N)			MSEtot
		$\bar{F}_x^M$	$\bar{F}_x^E$	$(\bar{F}_x^M - \bar{F}_x^E)^2$	$\bar{F}_y^M$	$\bar{F}_y^E$	$(\bar{F}_y^M - \bar{F}_y^E)^2$	
AZ31 Mg-alloy	600	21.1	18.6	6.25	21.3	19.7	2.56	
	1200	19.2	16.3	8.41	20.9	18.6	5.29	
	3000	17.4	13.6	14.44	20.7	16.8	15.21	
		MSE_x		9.7	MSE_y		7.69	17.39
Ti6Al4V alloy	600	168.6	146.1	506.25	223.7	196	767.29	
	1200	117.8	94.5	542.89	176	146.7	858.49	
	3000	112	85.7	691.69	140.2	109.3	954.81	
		MSE_x		580.28	MSE_y		860.2	1440.4

8. Conclusions

In this research, an experimental investigation and a mechanistic prediction of the cutting forces for conventional-speed milling with the tool runout have been presented. In particular, the influences of tool geometry, workpiece material and process parameters such as spindle speed, tool engagement and cutting direction were considered. The lower spindle speed produces larger cutting forces, and the amplitudes of the predicted cutting forces under lower spindle speed agree better with the measured values. However, in the case of higher speed, the predicted cutting forces deviate from those obtained experimentally since dynamic phenomena appear with increasing spindle speed. Accordingly, the rigid tool assumption drastically limits the predictive capacity of the model to the low spindle speeds. In conventional-speed milling, AZ31 Mg-alloy provides higher cutting force prediction accuracy than Ti6Al4V alloy. Also, the helix angle has a significant effect on the cutting forces, particularly the transverse force at the spindle speed of 600 rev/min. In the rigid end milling process, the tool runout causes a considerable variation in the cutting force curve over the rotation of the four-flute tool. The flutes on the high side of cutting tool with runout encounter larger force peaks than those on the other side. Thus, the runout effect should be taken into account to analyze the cutting forces in end milling. In addition, the force coefficients can be identified as constant values with respect to the variation of spindle speed for a particular tool-workpiece pair. Since the shearing mechanism changes with increasing spindle speed, there is a tendency to decrease especially in cutting force coefficients. The edge coefficients are greatly independent of tool geometry.

Disclosure statement

The authors declare that they have no known competing financial interests or personal relationships that could have appeared to influence the work reported in this paper.

References

Adem, K. A. M., R. Fales, and A. S. El-Gizawy. 2015. Identification of cutting force coefficients for the linear and nonlinear force models in end milling process using average forces and optimization technique methods. *The International Journal of Advanced Manufacturing Technology* 79 (9–12):1671–87. doi:10.1007/s00170-015-6935-3.

Altintas, Y. 2000. Modeling approaches and software for predicting the performance of milling operations at MAL-UBC. *Machining Science and Technology* 4 (3):445–78. doi:10.1080/10940340008945718.

Armarego, E. J. A., and N. P. Deshpande. 1993. Force prediction models and CAD/CAM software for helical tooth milling processes. I. Basic approach and cutting analysis. *International Journal of Production Research* 31 (8): 1991–2009. doi:10.1080/00207549308956836.

Aydın, M., and U. Köklü. 2017. Identification and modeling of cutting forces in ball-end milling based on two different finite element models with Arbitrary Lagrangian Eulerian technique. *The International Journal of Advanced Manufacturing Technology* 92 (1–4):1465–80. doi:10.1007/s00170-017-0229-x.

Aydın, M., and U. Köklü. 2020. Analysis of flat-end milling forces considering chip formation process in high-speed cutting of Ti6Al4V titanium alloy. *Simulation Modelling Practice and Theory* 100:102039. doi:10.1016/j.simpat.2019.102039.

Aydın, M., M. Uçar, A. Cengiz, and M. Kurt. 2015. Identification of static surface form errors from cutting force distribution in flat-end milling processes. *Journal of the Brazilian Society of Mechanical Sciences and Engineering* 37 (3):1001–13. doi:10.1007/s40430-014-0224-1.

Aydın, M., M. Uçar, A. Cengiz, M. Kurt, and B. Barkın. 2014. A methodology for cutting force prediction in side milling. *Materials and Manufacturing Processes* 29 (11–12):1429–35. doi:10.1080/10426914.2014.912315.

Budak, E., Y. Altıntaş, and E. J. A. Armarego. 1996. Prediction of milling force coefficients from orthogonal cutting data. *Journal of Manufacturing Science and Engineering* 118 (2):216–24. doi:10.1115/1.2831014.

Dikshit, M. K., A. B. Puri, and A. Maity. 2017. Analysis of cutting force coefficients in high-speed ball end milling at varying rotational speeds. *Machining Science and Technology* 21 (3):416–35. doi:10.1080/10910344.2017.1284562.

Ehman, K. F., S. G. Kapoor, R. E. DeVor, and I. Lazoglu. 1997. Machining process modeling: A review. *Journal of Manufacturing Science and Engineering* 119 (4B):655–63. doi:10.1115/1.2836805.

Grossi, N., L. Sallese, A. Scippa, and G. Campatelli. 2015. Speed-varying cutting force coefficient identification in milling. *Precision Engineering* 42:321–34. doi:10.1016/j.precisioneng.2015.04.006.

Hong, D., S. Kim, W. C. Choi, and J.-B. Song. 2003. Analysis of machining stability for a parallel machine tool. *Mechanics Based Design of Structures and Machines* 31 (4):509–28. doi:10.1081/SME-120023169.

Islam, M. N., H. U. Lee, and D. W. Cho. 2008. Prediction and analysis of size tolerances achievable in peripheral end milling. *The International Journal of Advanced Manufacturing Technology* 39 (1-2):129–41. doi:10.1007/s00170-007-1188-4.

Kline, W. A., and R. E. DeVor. 1983. The effect of runout on cutting geometry and forces in end milling. *International Journal of Machine Tool Design and Research* 23 (2–3):123–40. doi:10.1016/0020-7357(83)90012-4.

Kumanchik, L. M., and T. L. Schmitz. 2007. Improved analytical chip thickness model for milling. *Precision Engineering* 31 (3):317–24. doi:10.1016/j.precisioneng.2006.12.001.

Li, H. Z., and X. P. Li. 2005. A numerical study of the effects of cutter runout on milling process geometry based on true tooth trajectory. *The International Journal of Advanced Manufacturing Technology* 25 (5–6):435–43. doi:10.1007/s00170-003-1874-9.

Li, X. P., and H. Z. Li. 2004. Theoretical modelling of cutting forces in helical end milling with cutter runout. *International Journal of Mechanical Sciences* 46 (9):1399–414. doi:10.1016/j.ijmecsci.2004.07.001.

Lu, X., Z. Jia, F. Wang, G. Li, L. Si, and L. Gao. 2018. Model of the instantaneous undeformed chip thickness in micro-milling based on tooth trajectory. *Proceedings of the Institution of Mechanical Engineers, Part B: Journal of Engineering Manufacture* 232 (2):226–39. doi:10.1177/0954405416639890.

Mackerle, J. 2003. Finite element analysis and simulation of machining: An addendum: A bibliography (1996–2002). *International Journal of Machine Tools and Manufacture* 43 (1):103–14. doi:10.1016/S0890-6955(02)00162-1.

Maurel-Pantel, A., M. Fontaine, G. Michel, S. Thibaud, and J. C. Gelin. 2013. Experimental investigations from conventional to high speed milling on a 304-L stainless steel. *The International Journal of Advanced Manufacturing Technology* 69 (9–12):2191–213. doi:10.1007/s00170-013-5159-7.

Montgomery, D., and Y. Altintas. 1991. Mechanism of cutting force and surface generation in dynamic milling. *Journal of Engineering for Industry* 113 (2):160–8. doi:10.1115/1.2899673.

Rubeo, M. A., and T. L. Schmitz. 2016. Mechanistic force model coefficients: A comparison of linear regression and nonlinear optimization. *Precision Engineering* 45:311–21. doi:10.1016/j.precisioneng.2016.03.008.

Sutherland, J. W., and R. E. DeVor. 1986. An improved method for cutting force and surface error prediction in flexible end milling systems. *Journal of Engineering for Industry* 108 (4):269–79. doi:10.1115/1.3187077.

Tlusty, J. 2000. *Manufacturing processes and equipment*. Hoboken, NJ: Prentice Hall.

Wang, C., P. Ding, X. Huang, and H. Li. 2021. A method for predicting ball-end cutter milling force and its probabilistic characteristics. *Mechanics Based Design of Structures and Machines.* Advance Online Publication. doi:10.1080/15397734.2021.1927752.

Wang, J. J., and S. Y. Liang. 1996. Chip load kinematics in milling with radial cutter runout. *Journal of Engineering for Industry* 118 (1):111–6. doi:10.1115/1.2803631.

Wan, M., Y. C. Ma, J. Feng, and W. H. Zhang. 2016. Study of static and dynamic ploughing mechanisms by establishing generalized model with static milling forces. *International Journal of Mechanical Sciences* 114:120–31. doi:10.1016/j.ijmecsci.2016.05.010.

Wan, M., and W. H. Zhang. 2006. Calculations of chip thickness and cutting forces in flexible end milling. *The International Journal of Advanced Manufacturing Technology* 29 (7–8):637–47. doi:10.1007/s00170-005-2572-6.

Wan, M., W. H. Zhang, J. W. Dang, and Y. Yang. 2010. A novel cutting force modelling method for cylindrical end mill. *Applied Mathematical Modelling* 34 (3):823–36. doi:10.1016/j.apm.2009.09.012.

Wan, M., W. H. Zhang, G. Tan, and G. H. Qin. 2007. New algorithm for calibration of instantaneous cutting-force coefficients and radial run-out parameters in flat end milling. *Proceedings of the Institution of Mechanical Engineers, Part B: Journal of Engineering Manufacture* 221 (6):1007–19. doi:10.1243/09544054JEM515.

Wojciechowski, S. 2015. The estimation of cutting forces and specific force coefficients during finishing ball end milling of inclined surfaces. *International Journal of Machine Tools and Manufacture* 89:110–23. doi:10.1016/j.ijmachtools.2014.10.006.

Yalcin, C. 2009. Milling cutter software architecture for force and surface finish modeling., PhD diss., University of New Hampshire.

Zhang, X., T. Yu, and W. Wang. 2019. Cutting forces modeling for micro flat end milling by considering tool run-out and bottom edge cutting effect. *Proceedings of the Institution of Mechanical Engineers, Part B: Journal of Engineering Manufacture* 233 (2):470–85. doi:10.1177/0954405417726811.